catalysts

MDPI

Article

Effects of Synthesis Variables on SAPO-34 Crystallization Templated Using Pyridinium Supramolecule and Its Catalytic Activity in Microwave Esterification Synthesis of Propyl Levulinate

Yik-Ken Ma [1], Taghrid S. Alomar [2], Najla AlMasoud [2], Zeinhom M. El-Bahy [3], Stephen Chia [4], T. Jean Daou [5,6], Fitri Khoerunnisa [7], Tau Chuan Ling [8,*] and Eng-Poh Ng [1,*]

1 School of Chemical Sciences, Universiti Sains Malaysia, USM, Penang 11800, Malaysia
2 Department of Chemistry, College of Science, Princess Nourah bint Abdulrahman University, P.O. Box 84428, Riyadh 11671, Saudi Arabia
3 Department of Chemistry, Faculty of Science, Al-Azhar University, Nasr City, Cairo 11884, Egypt
4 Centre for Global Archaeological Research, Universiti Sains Malaysia, USM, Penang 11800, Malaysia
5 Axe Matériaux à Porosités Contrôlées, Institut de Science de Matériaux de Mulhouse UMR 7361, ENSCMu, Université de Haute-Alsace, 3b Rue Alfred Werner, 68093 Mulhouse, France
6 Université de Strasbourg, 67000 Strasbourg, France
7 Chemistry Education Department, Universitas Pendidikan Indonesia, Jl. Setiabudhi 258, Bandung 40514, Indonesia
8 Institute of Biological Sciences, Faculty of Science, University of Malaya, Kuala Lumpur 50603, Malaysia
* Correspondence: tcling@um.edu.my (T.C.L.); epng@usm.my (E.-P.N.)

Citation: Ma, Y.-K.; Alomar, T.S.; AlMasoud, N.; El-Bahy, Z.M.; Chia, S.; Daou, T.J.; Khoerunnisa, F.; Ling, T.C.; Ng, E.-P. Effects of Synthesis Variables on SAPO-34 Crystallization Templated Using Pyridinium Supramolecule and Its Catalytic Activity in Microwave Esterification Synthesis of Propyl Levulinate. *Catalysts* **2023**, *13*, 680. https://doi.org/10.3390/catal13040680

Academic Editors: De Fang, Yun Zheng and Mingjun Jia

Received: 27 February 2023
Revised: 27 March 2023
Accepted: 27 March 2023
Published: 30 March 2023

Abstract: A detailed investigation of the hydrothermal crystallization of SAPO-34 in the presence of the novel 1-propylpyridinium hydroxide ([PrPy]OH) organic structural directing agent is presented. The synthesis conditions are systematically tuned to investigate the effects of various parameters (viz. concentrations of each reactant, crystallization time, and temperature) on the nucleation and crystallization of SAPO-34. The results show that a careful variation in each of the synthesis parameters results in the formation of competing phases such as SAPO-5, SAPO-35, and SAPO-36. Pure and fully crystalline SAPO-34 can be crystallized using a precursor hydrogel of a molar ratio of 2.0 Al: 4.7 P: 0.9 Si: 6.7 [PrPy]OH: 148 H_2O at 200 °C for only 19 h, which is a shorter time than that found in previous studies. The prepared SAPO-34 is also very active in the esterification of levulinic acid and 1-propanol. By using microwave heating, 91.5% conversion with 100% selectivity toward propyl levulinate is achieved within 20 min at 190 °C. Hence, the present study may open a new insight into the optimum synthesis study of other zeolites using novel pyridinium organic moieties and the opportunity of replacing conventional harmful and non-recyclable homogeneous catalysts in levulinate biofuel synthesis.

Keywords: SAPO-34; zeolites; crystallization; esterification; propyl levulinate

1. Introduction

Aluminophosphates (AlPO-*n*) and silicoaluminophosphates (SAPO-*n*) are zeolite-like microporous solids that have shown numerous promising industrial applications in adsorption, ion exchange, and catalysis [1–3]. Among them, SAPO-34 (CHA topology), which has a three-dimensional pore system with a diameter size of 3.80 × 3.80 $Å^2$ and a large CHA cage (9.4 Å in diameter), is one of the most important zeolites and has widely been used in the methanol-to-olefins (MTO), gas separation, and hydroisomerization reactions [4,5].

In general, several strategies can be used to crystallize SAPO-34, namely the hydrothermal technique [6], interzeolite conversion [7], and dry gel conversion [8]. During

the crystallization process, aliphatic or aromatic amines, such as diethylamine [9], triethylamine [10], tetraethylammonium hydroxide [11], piperidine [12], or morpholine [13], are added and served as structure-directing agents (SDAs) to direct the crystallization of SAPO-34 zeolite. However, the classical time-consuming hydrothermal treatment may severely impact the scale-up production and cost, where the shortest crystallization time for the formation of SAPO-34 so far requires at least 24 h at 200 °C [9,12,13]. In addition, the use of various types and amounts of SDAs with different electronic and hydrophilic/hydrophobic properties in SAPO-34 synthesis also leads to an alteration in the colloidal properties, and thermodynamic stability and activity of the precursor hydrogel, which in turn affects the overall nucleation and crystallization kinetics, final phase purity, chemical composition, crystal size, and morphology of the synthesized zeolites [14,15]. Therefore, a detailed study of synthesis variables via hydrothermal condition improvement is of utmost importance for enabling comprehensive control of the zeolite crystallization process.

Pyridinium-based molecules are a new type of SDA that, thus far, have seldom been synthesized and used in the preparation of zeolites. Due to their unique aromatic structure, delocalization of π electrons, and presence of electronegative N atom in the cyclic ring, pyridinium-based SDAs show different polarity, surface charge, and electron density compared to aliphatic aminic SDAs, which may lead to different crystallization profiles of zeolites (particularly in SAPO-34) [16]. In addition, other synthesis parameters, such as the concentrations of various reactants, crystallization time, and temperature, also directly affect the thermodynamic and crystallization process of zeolites [17,18]. Nevertheless, knowledge about the effects of these parameters on the crystallization of SAPO-34 in the presence of pyridinium-based SDA still remains limited.

In order to better understand the crystallization phenomenon of SAPO-34 and the roles of synthesis variables in the formation of SAPO-34 in the presence of heterocyclic pyridinium SDA, a systematic set of experiments is performed. Specifically, 1-propylpyridinium is first prepared prior to being applied in the hydrothermal crystallization of SAPO-34. Concurrently, a study of the influence of crystallization conditions by altering the synthesis parameters is also carried out. Finally, the acidity and surface properties of SAPO-34 crystals are studied before being tested in the production of propyl levulinate biofuel additive via the esterification of levulinic acid and propanol using a microwave heating method.

2. Results and Discussion

2.1. Single-Parameter Tuning Synthesis of SAPO-34

2.1.1. Time-Dependent Formation Study of SAPO-34

Ostwald's Law of successive reaction is frequently invoked in the formation of zeolitic materials where successive phase transformations into more thermodynamically stable zeolite phases occur due to their metastability. As such, the effect of crystallization time was studied by heating the hydrogel of a molar composition of 2.0 Al: 4.7 P: 0.9 Si: 6.7 [PrPy]OH: 148 H_2O for 0, 6, 12, 16, 19, and 30 h at 200 °C. Initially, at 0 h, the hydrogel is amorphous indicating no crystalline phase is formed upon completion of hydrogel preparation (Table 1). The white hydrogel is subjected to hydrothermal treatment to allow chemical reactions (dissolution, polymerization, induction, nucleation, crystallization, etc.) to occur. The white suspension solid dissolves entirely in the mother liquor after 6 h of heating, indicating the formation of monomeric and oligomeric Si, P, and Al oxides in the mother liquor [19].

The precursor hydrogel is further heated for 12 h where a small amount of soft solid is recovered upon centrifugation. The solid displays an irregular shape according to the FESEM analysis, proving its XRD amorphous characteristics (Figure 1a). Hence, it reveals that polymerization of Si, Al, and P oligomers has occurred, leading to the sedimentation of a dense amorphous solid. Nucleation is witnessed at 16 h where several XRD peaks corresponding to SAPO-34 slowly appear (Figure 1b). The solid comprises cubic SAPO-34 crystals with rough surfaces covered by amorphous entities.

Table 1. The porous and acidity properties of SAPO-34 (S-3) crystallized using [PrPy]OH.

Sample	Si/(P + Al) Ratio	S_{BET} (m^2 g^{-1}) [a]	S_{Micro} (m^2 g^{-1}) [b]	V_{Total} (cm^3 g^{-1}) [c]	NH_3-TPD (mmol g^{-1})		
					Weak-to-Medium [d]	Mild-to-Strong [e]	Total
S-3	0.24	673	661	0.27	1.27	1.25	2.52

[a] Specific surface area; [b] Micropore surface area; [c] Total pore volume; [d] Calculated based on TPD desorption curves at 168 °C and 235 °C; [e] Calculated based on desorption curves at 404 °C and 479 °C.

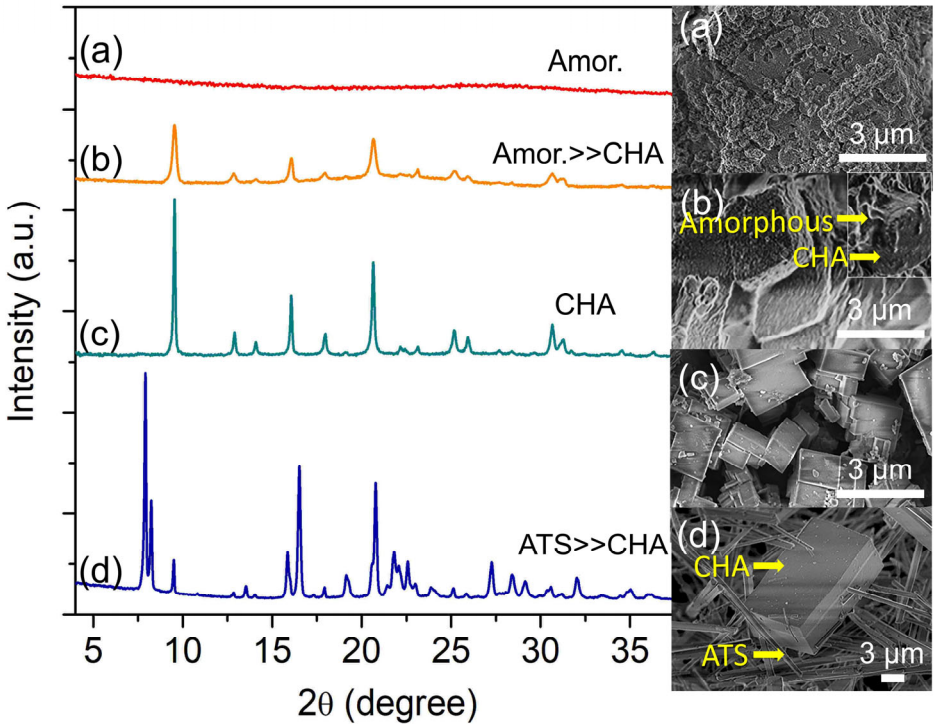

Figure 1. XRD patterns and FESEM micrographs of (**a**) S-1, (**b**) S-2, (**c**) S-3, and (**d**) S-4 solids heated at 150 °C for 12 h, 16 h, 19 h, and 30 h, respectively.

Further extending the crystallization time to 19 h confirms the complete formation of SAPO-34 where the amorphous solid is entirely consumed for the crystal growth, leading to well-defined cubic crystals with sharp edges (ca. 1.86 µm) (Figure 1c). As shown in Figure 1, the XRD diffraction peaks corresponding to SAPO-34 crystallites (9.48° [100], 16.06° [11-1], 17.93° [111], 18.86° [200], 20.62° [20-1]) are intense and no additional peaks are observed, reflecting its high crystallinity and purity.

The crystallization time is further extended to 30 h to study the metastable phase formation. As seen in Figure 1, the main XRD peaks of SAPO-34 at 2θ = 9.49° "100", 18.86° "200", and 17.93° "111" are becoming weaker, and they are at the expense of the peaks of SAPO-36 (2θ = 7.90° "110", 8.24° "020", 15.86° "220", 16.52° "040", and 20.78° "310") (Figure 1d). The intrazeolite transformation process is also detected by FESEM analysis whereby the cuboid-shaped crystals (SAPO-34) are co-crystallized together with needle-like crystals (SAPO-36), hence confirming the metastability feature of SAPO-34.

2.1.2. Effect of P/Al Molar Ratio

Phosphoric acid plays a significant role in the crystallization of SAPO-34 since it is one of the basic building blocks of the zeolite. It also alters the pH of the hydrogel that governs the entire crystallization process [20]. Hence, the effect of phosphoric acid amount (presented in the form of P/Al molar ratio) is investigated by heating the precursor hydrogel of 2.0 Al: *w* P: 0.9 Si: 6.7 [PrPy]OH: 148 H_2O (*w* = 4.1, 4.7, 5.3 and 5.9) at 200 °C for 19 h. Amorphous particles are obtained when *w* = 4.1 (P/Al = 2.05) (Figure 2a) due to

weakly alkaline hydrogel (pH = 7.2) that inhibits the nucleation of SAPO-34 [21]. When the P/Al ratio increases to 2.35 (w = 4.7), the pH of the precursor gel drops to 6.7. Under this weakly acidic condition, SAPO-34 crystals with conventional cubic morphology (ca. 1.86 μm) are formed (Figure 2b).

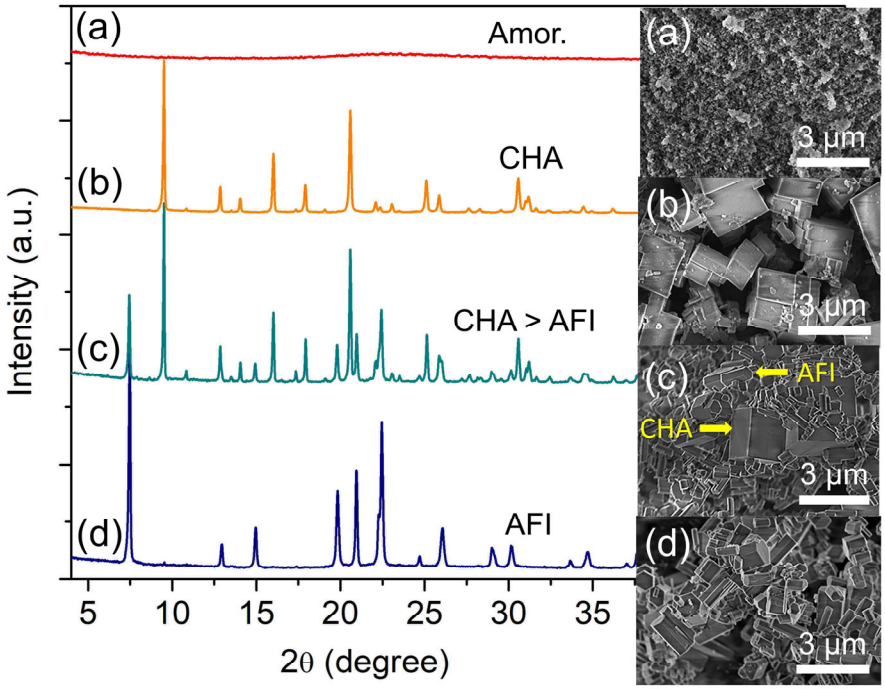

Figure 2. XRD patterns and FESEM micrographs of (**a**) S-5 (w = 4.1), (**b**) S-3 (w = 4.7), (**c**) S-6 (w = 5.3), and (**d**) S-7 (w = 5.9) samples. The samples were prepared using a hydrogel of 2.0 Al: w P: 0.9 Si: 6.7 [PrPy]OH: 148 H_2O heated at 200 °C for 19 h.

Further adding phosphoric acid increases the acidity of the precursor hydrogel (pH 6.2 when w = 5.3, and pH 5.6 when w = 5.9) which also witnesses the interzeolite transformation of SAPO-34 into SAPO-5 whereby the latter zeolite phase is preferentially formed under acidic conditions (Figure 2c,d) [22]. As shown, SAPO-5 (2θ = 7.47° "100", 19.85° "210", 20.97° "002", 22.46° "300") is formed at the expense of SAPO-34 where the metastable SAPO-34 particles are partially disintegrated in the mother liquor, releasing double 6-ring (D6R) secondary building units—the seeding sites—for the crystallization of SAPO-5 [23]. Furthermore, the mild acidic hydrogel (pH = 5.0–6.0) at w = 5.9 also favors the formation of SAPO-5, producing a hexagonal prism of crystals with sharp edges and smooth surfaces (ca. 1.16 × 1.25 μm^2).

2.1.3. Effect of Si Content

Silicon (Si) is another important parameter since it is the origin of the acid sites of SAPO-34 besides altering the entire crystallization process [24,25]. Hence, the effects of Si content on the formation of SAPO-34 were studied by heating the hydrogel of molar composition 2.0 Al: 4.7 P: x Si: 6.7 [PrPy]OH: 148 H_2O (x = 0, 0.4, 0.9 and 1.3) at 200 °C for 19 h. The XRD analysis reveals that the sample without the addition of Si is identified as an aluminophosphate (AlPO) clay solid with a thin layered morphology (ca. 1.78 × 0.04 μm^2) (Figure 3a). At x = 0.4, the clay material completely transforms into pure SAPO-36 (ATS topology)—a 12-membered ring large pore zeolite with needle-like shape (ca. 9.18 μm)—based on the major diffraction peaks at 2θ = 7.90° "110", 8.29° "020", 15.81° "220", 16.41° "040", and 20.67° "310" (Figure 3b) [23].

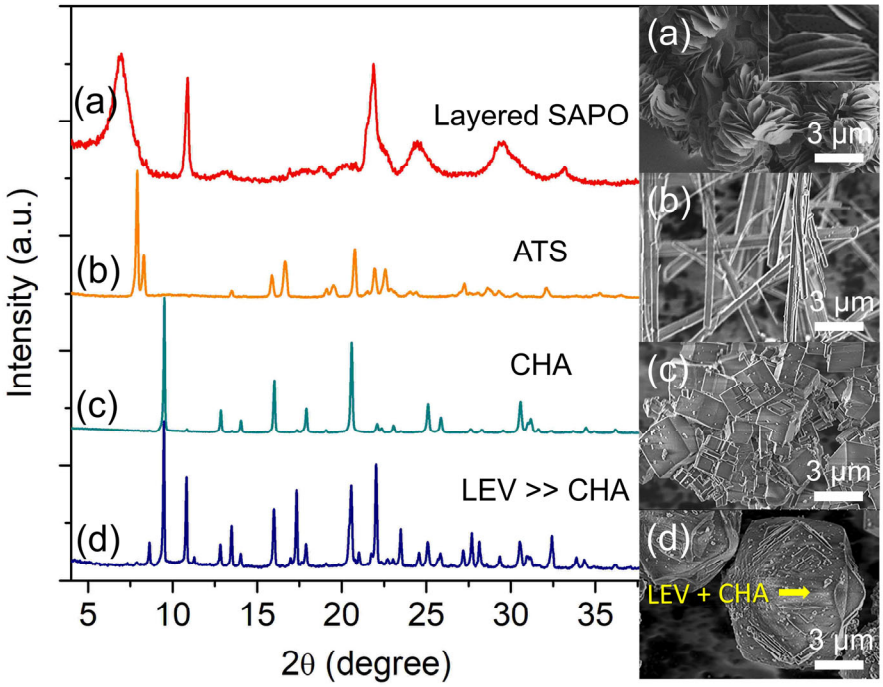

Figure 3. XRD patterns and FESEM micrographs of (**a**) S-8 (x = 0), (**b**) S-9 (x = 0.4), (**c**) S-3 (x = 0.9), and (**d**) S-10 (x = 1.3) samples. The samples were prepared using the hydrogel of 2.0 Al: 4.7 P: x Si: 6.7 [PrPy]OH: 148 H_2O heated at 200 °C for 19 h.

When the Si content is slightly increased to x = 0.9, the phase transformation from needle-like SAPO-36 into cuboid SAPO-34 crystallites (1.86 μm) is observed, thus showing the active participation of Si in the framework rearrangement process (Figure 3c). With further slightly increasing the Si content to x = 1.3, a partial transformation of cuboid SAPO-34 (7.5 μm) into rhombohedral SAPO-35 (7.9 μm, LEV topology) occurs. This is proven by the several SAPO-35 XRD major peaks (2θ = 8.63° "101", 10.82° "012", 13.49° "110", 17.33° "202", and 21.98° "122") that co-exist with those of SAPO-34 (Figure 3d) [23]. Thus, the results suggest that besides the active involvement of Si atoms as building blocks for self-organization, the mother liquor of SAPO-34 might contain double 6-rings (D6R) secondary building units too which can act as secondary seeds for further promoting SAPO-35 transformation (note: ATS, CHA, and LEV-type microporous solids have the same D6R secondary building units) [26].

2.1.4. Effect of [PrPy]OH Content

Four precursor mixtures (2.0 Al: 4.7 P: 0.9 Si: y [PrPy]OH: 148 H_2O) with different amounts of [PrPy]OH (y = 5.3, 6.0, 6.7, and 7.4) were hydrothermally heated at 200 °C for 19 h and the initial pH of the mixture was also measured. When y = 5.3, a mildly acidic hydrogel is formed (pH 5.76), which leads to the crystallization of pure SAPO-5 crystals with a hexagonal prism rod shape (ca. 0.70 × 1.18 μm^2) (Figure 4a) [27]. Partial transformation of SAPO-5 into SAPO-34 is detected when the amount of [PrPy]OH organic template increases to y = 6.0 (Figure 4b). At this point, the pH becomes nearly neutral (pH = 6.31). As shown in the XRD pattern, SAPO-5 (2θ = 7.45° "100", 12.92° "110", 14.97° "200", 19.85° "210", 20.97° "002", and 22.44° "300") remains as the major crystalline phase over SAPO-34 (2θ = 9.51° "100", 16.06° "11-1", 17.94° "111", 20.62° "20-1") in line with the FESEM observation; SAPO-5 hexagonal prismatic crystals are intergrown on the cuboid SAPO-34 crystals. Hence, increasing the hydrogel pH (by increasing the template concentration) is beneficial for inducing the crystallization of SAPO-34.

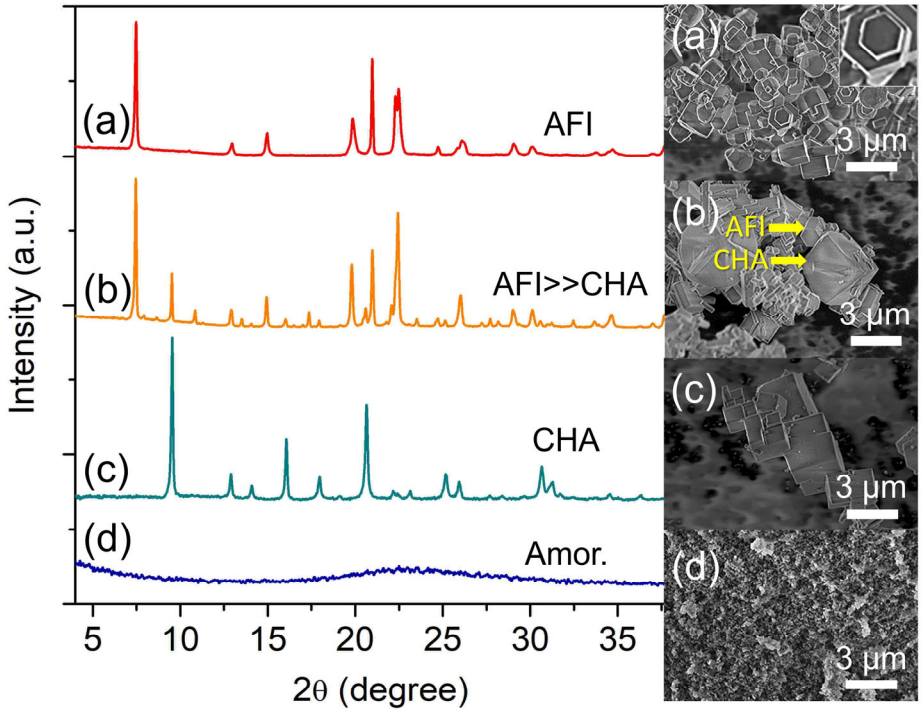

Figure 4. XRD patterns and FESEM micrographs of (**a**) S-11 (y = 5.3), (**b**) S-12 (y = 6.0), (**c**) S-3 (y = 6.7), and (**d**) S-13 (y = 7.4) samples. The samples were prepared using the hydrogel of 2.0 Al: 4.7 P: 0.9 Si: y [PrPy]OH: 148 H_2O heated at 200 °C for 19 h.

The above speculation is proven when the pH of the hydrogel is adjusted to be very close to neutral (pH = 6.67, y = 6.7) where fully crystalline cuboid SAPO-34 crystals (ca. 1.33 μm) are formed (Figure 4c). However, further increasing the template content to x = 7.4 (pH = 7.12) leads to the amorphization of the sample. Thus, the results demonstrate that $[PrPy]^+$ supramolecule (dimensional size of 6.8 × 3.2 $Å^2$) helps in the formation of pore framework structures of SAPO-5 and SAPO-34 via stabilizing their respective 12-membered rings (7.3 × 7.3 × 7.3 $Å^3$) and 8-membered rings (3.8 × 3.8 × 3.8 $Å^3$) through side-on and head-on orientations [24,28]. Furthermore, the addition of $[PrPy]^+$ template in OH^- form also controls the pH of the hydrogel by providing a suitable environment for promoting nucleation for crystallizing SAPO-5 and SAPO-34 materials [29].

2.1.5. Effect of H_2O Content

Water content is one of the important components in precursor hydrogel as it controls the concentration of reactants besides serving as the solvent in the hydrothermal synthesis of zeolite [30]. As such, the effect of water content on the crystallization of SAPO-34 was studied at 200 °C for 19 h by varying the amount of water in the hydrogel of 2.0 Al: 4.7 P: 0.9 Si: 6.7 [PrPy]OH: z H_2O (z = 116, 148, 180, 240). From the experimental observation, the crystallization condition is very sensitive to the water content. By varying the amount of water, several competing phases, such as SAPO-36 (ATS), SAPO-35 (LEV), SAPO-34 (CHA), and SAPO-5 (AFI), are detected. For instance, at z = 116, SAPO-36 forms as the competing phase to SAPO-34 (Figure 5a) where the large cuboid SAPO-34 crystals (ca. 6.7 μm) are grown with their surface covered by short needle-shaped crystals of SAPO-36 (ca. 1.1 μm). The SAPO-36 phase, however, disappears at z = 148, forming only pure SAPO-34 as the final product (Figure 5b). As seen, the crystallites are almost homogeneous and have uniform size distribution (ca. 1.86 μm) due to the effects of water in altering the intermolecular forces and supersaturation condition of the precursor [31].

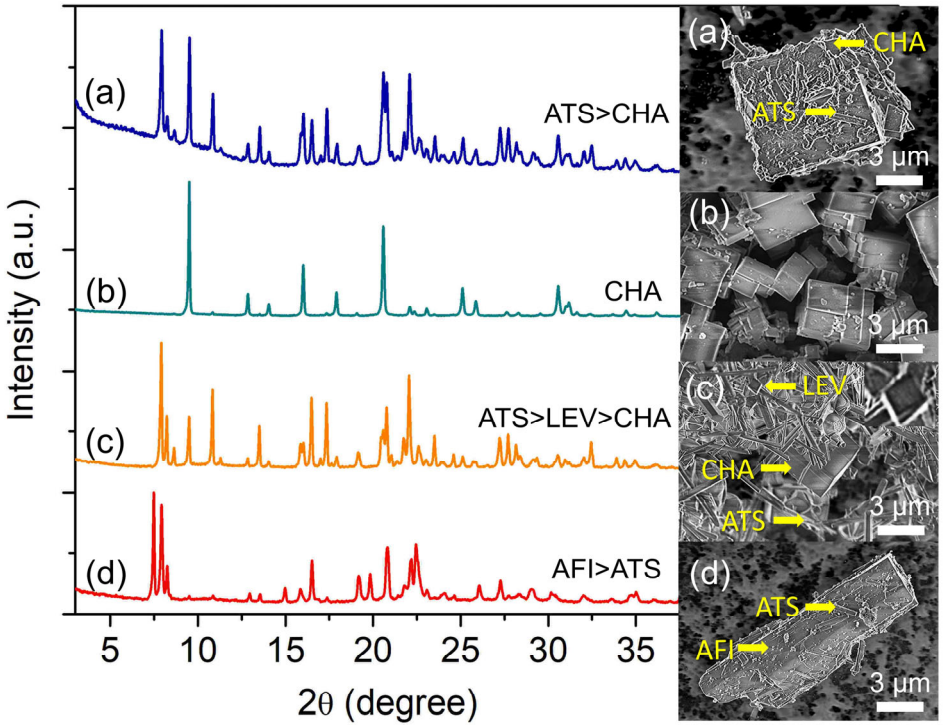

Figure 5. XRD patterns and FESEM micrographs of (**a**) S-14 (*z* = 116), (**b**) S-3 (*z* = 148), (**c**) S-15 (*z* = 180), and (**d**) S-16 (*z* = 240) samples. The samples were prepared using the hydrogel of 2.0 Al: 4.7 P: 0.9 Si: 6.7 [PrPy]OH: *z* H_2O heated at 200 °C for 19 h.

Increasing the water content to *z* = 180 witnesses the re-appearance of SAPO-36 (needle-like shape) where SAPO-35 (rhombohedral shape) together with SAPO-34 (cubic shape) exist as the minor phase (Figure 5c). The main diffraction peaks related to SAPO-36 are observed at 2θ = 7.90° "110", 8.18° "020", and 16.43° "040", whereas those of SAPO-35 and SAPO-34 are respectively found at 2θ = 10.84° "012" and 9.49° "100". However, SAPO-5 (2θ = 7.49° "100", 20.82° "002", and 22.38° "211") appears as the major phase over SAPO-36 when more water is added (*z* = 240) (Figure 5d) because, at high water content, the hydrogel becomes more acidic which favors the crystallization of SAPO-5 [32]. A similar effect is also detected by the FESEM analysis whereby needle-like SAPO-36 crystals are grown on the surface of large rod-like SAPO-5 crystals.

Compared to other synthesis parameters, water content is less selective in controlling the zeolite phases because water is used as a solvent for dissolving reactants and at the same time, transporting nutrients to the inorganic matrices for nucleation and crystal growth during hydrothermal synthesis [33]. The presence of different amounts of water and autogenic pressure generated from water vapor at high temperatures also tend to alter the nutrient concentration and solubility, which indirectly affect the supersaturation profile of the zeolites. As a result, the resulting final products with multiple phases are observed [34].

2.1.6. Effect of Crystallization Temperature

The heating temperature is the most important synthesis parameter since energy is essential for chemical reactions (e.g., polycondensation, nucleation, crystallization, etc.) to occur [35]. Hence, the effect of heating temperature on the crystallization of SAPO-34 was studied by heating the hydrogels of 2.0 Al: 4.7 P: 0.9 Si: 6.7 [PrPy]OH: 148 H_2O at 160, 180, 200, and 220 °C for 19 h. At 160 °C, the sample is amorphous according to XRD analysis, but few cuboid crystallites (ca. 0.8 μm) can be seen amid spherical amorphous entities indicating that nucleation of SAPO-34 has occurred at 160 °C (Figure 6a). By increasing the temperature to 180 °C, it is possible to see more SAPO-34 crystals are formed which leads

to the emergence of weak X-ray diffraction peaks at 2θ = 9.51° "100", 16.05° "11-1", and 20.65° "20-1" (Figure 6b). As shown in Figure 6, the XRD peaks are broad, indicating small crystallites, which is confirmed by the FESEM data (ca. 1.1 μm) [24].

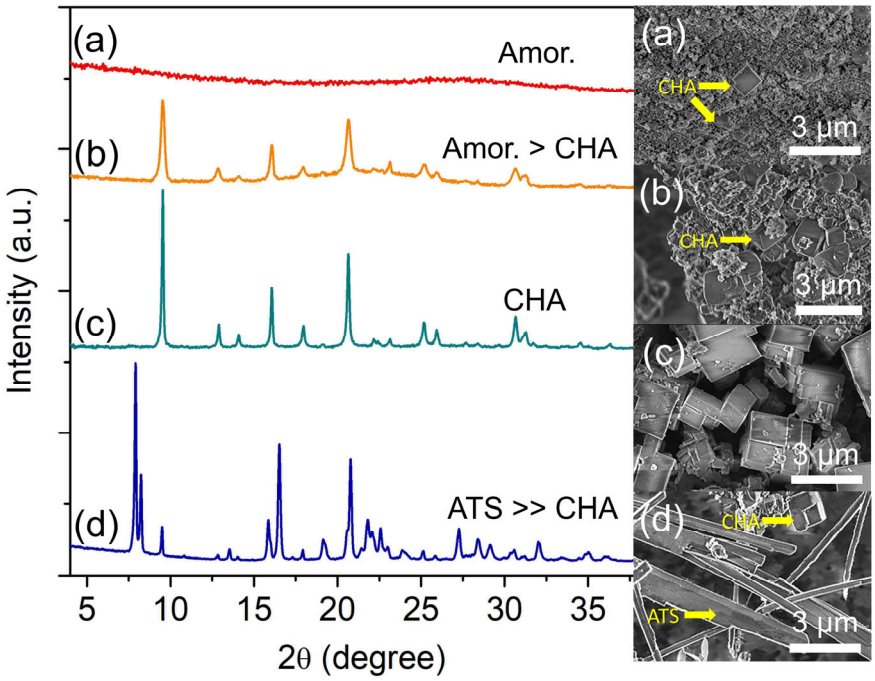

Figure 6. XRD patterns and FESEM micrographs of (**a**) S-17, (**b**) S-18, (**c**) S-3, and (**d**) S-19 samples prepared using the hydrogel of 2.0 Al: 4.7 P: 0.9 Si: 6.7 [PrPy]OH: 148 H_2O and heated at 160 °C, 180 °C, 200 °C and 220 °C for 19 h, respectively.

The crystallization and crystal growth rates are accelerated when increasing the heating temperature to 200 °C. As shown, only strong and narrow XRD diffraction peaks corresponding to SAPO-34 are seen. Furthermore, no amorphous hump is detected revealing that all amorphous particles have been consumed serving as nutrients for SAPO-34 formation [36]. The same phenomenon is also shown by FESEM analysis where large cuboid crystals (ca. 1.86 μm) without amorphous spherical particles are captured. However, a partial transformation of SAPO-34 (CHA topology, FD = 15.1 T/1000 $Å^3$) into SAPO-36 of a denser framework (ATS topology, FD = 16.1 T/1000 $Å^3$) is observed with heating temperature increases to 220 °C. As shown, the XRD results indicate SAPO-36 is formed at the expense of SAPO-34 where the needle-like structures (ca. 7.5 μm, SAPO-36) dominate the FESEM image over the cuboid SAPO-34 particles (Figure 6d). Hence, the results indicate that the crystallization of SAPO-34 zeolite is a thermally activated process. However, its metastable nature leads it to the transformation into another denser zeolite phase, especially at higher temperatures [37].

The TGA/DTG technique is used to prove the role of $[PrPy]^+$ as a supramolecular structure-directing agent on SAPO-34. Figure 7 shows the TGA/DTG thermogram of uncalcined SAPO-34 (S-3). The first stage of weight loss (7.3%) at below 200 °C is due to physisorbed water, the second weight loss (7.9%) at 200–566 °C is due to the decomposition of $[PrPy]^+$ molecules, while the third weight loss (1.0%) at 566–795 °C is due to carbon coke deposition from incomplete combustion of $[PrPy]^+$. As seen, the decomposition of $[PrPy]^+$ is delayed at higher temperatures due to the occlusion of $[PrPy]^+$ in the pores of SAPO-34. From the weight loss, it is found that one molecule of $[PrPy]^+$ is packed and enfolded by ca. 18 units of TO_2 primary building units (T = Si, Al, or P). It is believed that the occlusion of $[PrPy]^+$ adapts the "ship in a bottle" pathway where the TO_2 units polymerize around the $[PrPy]^+$ (3.2 Å × 6.8 Å × 2.5 Å) before the supramolecule is trapped inside the pores (3.8 Å × 3.8 Å) [28].

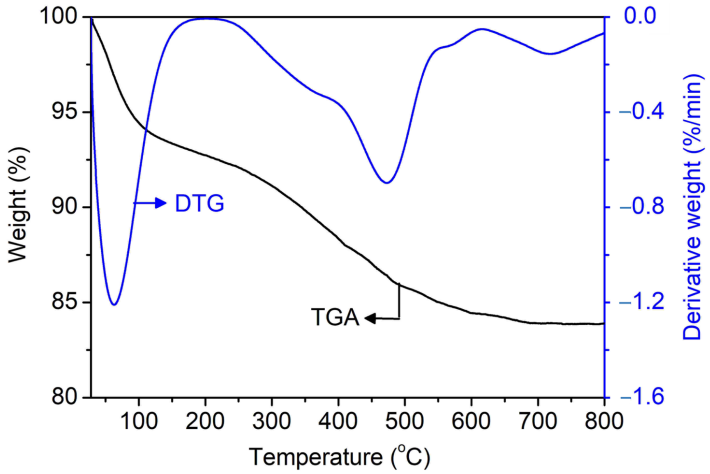

Figure 7. TGA/DTG thermograms of uncalcined SAPO-34 (S-3) sample.

2.2. Surface Characterizations of SAPO-34

The porosity of SAPO-34 crystallized using PrPy]OH supramolecule was studied using nitrogen adsorption-desorption analysis at −196 °C and the data is shown in Figure 8 and Table 1. The solid displays a type I curve shape without steep N_2 uptake at high P/P_o, indicating it merely has microporosity [38]. The solid has high porosity showing a high specific surface area (S_{BET} = 673 m^2 g^{-1}), micropore surface area (661 m^2 g^{-1}), and total pore volume (V_{Total} = 0.27 cm^3 g^{-1}). In addition, the SAPO-34 solid also exhibits moderate insertion of Si atoms (Si/(Al + P) ratio = 0.24) into the CHA zeolite framework resulting in the formation of surface acidity of different strengths (Table 1). As shown, the microporous solid possesses weak-to-medium (desorption curves at 168 °C and 235 °C) and medium-to-strong (desorption curves at 404 °C and 479 °C) acid sites arising from T–OH (T = Al, P, or Si) defect sites and framework tetrahedral Si sites, respectively [39]. The total number of acid sites of [PrPy]OH-synthesized SAPO-34 is found to be 2.52 mmol g^{-1} which is higher than that of the classical TEAOH-synthesized SAPO-34 (1.79 mmol g^{-1}) [11].

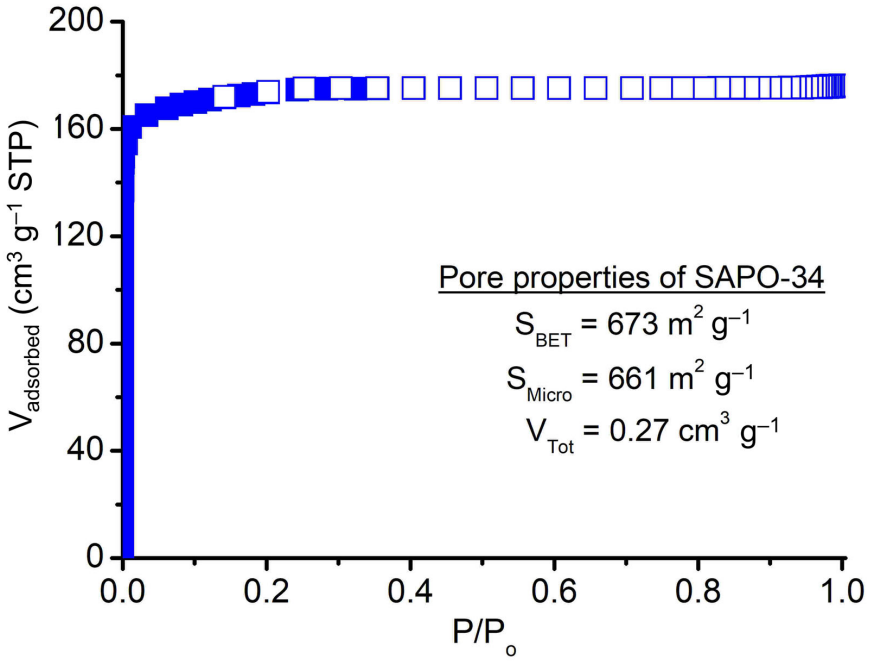

Figure 8. Nitrogen adsorption-desorption isotherm of SAPO-34 (S-3).

2.3. Catalytic Reaction Study

SAPO-34 zeolite is an important solid catalyst for chemical production and hence the catalytic behavior of SAPO-34 crystallized using [PrPy]OH was investigated in the microwave-assisted esterification of levulinic acid with 1-propanol. The reaction was first run at 130 °C without catalyst and no reaction conversion is observed after 60 min. This shows that microwave heating is inactive in the esterification reaction. When SAPO-34 zeolite is added, a significant increase in reaction conversion (60.6%) with 100% selectivity towards propyl levulinate is observed after 20 min of heating (Figure 9). The esterification conversion keeps increasing with the extension of the heating time and 82.2% of conversion is achieved at 60 min. Thus, the results show that SAPO-34 catalyst is active in this reaction whereby the catalytic activity of SAPO-34 comes from the $(P\text{-}O\text{-}Si\text{-}O\text{-}Al)^{-}H^{+}$ active sites located at the surface of the solid.

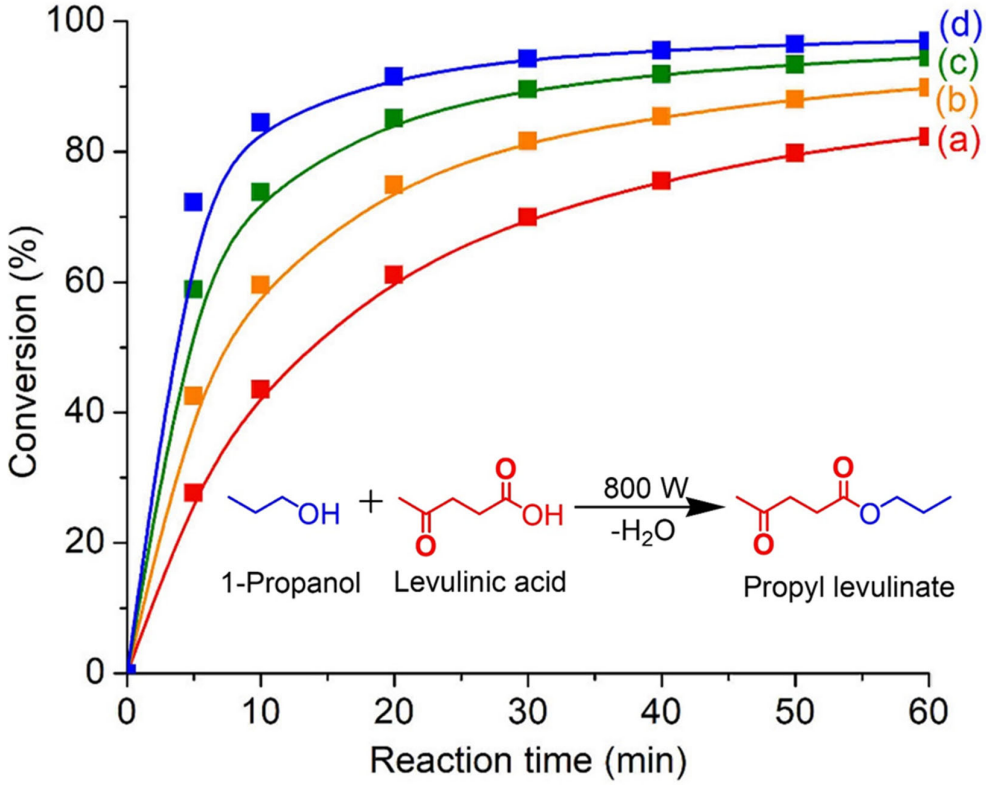

Figure 9. Microwave-assisted esterification of levulinic acid with 1-propanol in the presence of SAPO-34 (S-3) catalyst at (**a**) 130 °C, (**b**) 150 °C, (**c**) 170 °C, and (**d**) 190 °C for 60 min. Reaction conditions: Catalyst loading = 0.100 g; 1-propanol:levulinic acid molar ratio = 11:1; microwave power = 800 W; solvent-free.

The esterification reaction is also carried out at elevated temperatures (130–190 °C) over various times (0–60 min). As shown, a high reaction temperature is beneficial for the esterification of levulinic acid since the reaction kinetics are exponentially proportional to the temperature as shown by the Arrhenius theory [40]. For instance, the conversion is significantly enhanced from 60.6% to 91.2% when the temperature increases from 130 °C to 190 °C after 20 min of reaction. Thus, it is speculated that higher temperatures provide higher kinetic energy to the reactants (levulinic acid and 1-propanol) and the organic guest molecules are hence able to diffuse rapidly into the micropores of SAPO-34. The confinement environment of the zeolite then facilitates the orientation and chemisorption of reactants molecules, enabling the esterification to take place [41].

A catalytic comparative study between SAPO-34 and common homogeneous (e.g., sulfuric acid, hydrochloric acid, acetic acid) and heterogeneous (H-LTL, SAPO-18, H-FAU-Y) catalysts was also carried out (Figure 10, see Supplementary Materials: Table S1). All

heterogeneous catalysts are 100% selective to propyl levulinate, while medium pore SAPO-34 and SAPO-18 zeolites (>90%) show better performance than large pore H-LTL and H-FAU-Y (ca. 75.0%) zeolites. The better catalytic activity of SAPO-34 (3.8 × 3.8 × 3.8 $Å^3$) and SAPO-18 (3.8 × 3.8 × 3.6 $Å^3$) could be due to their higher acidity and small pores that can exhibit proximity effect, viz. allowing oriented molecular diffusion inside the narrow pores and organize the levulinic acid (2.49 × 5.98 × 1.78 $Å^3$) and 1-propanol (3.11 × 5.35 × 2.54 $Å^3$) molecules on the acid sites so that the reactants molecules are much closer together than they would be in large pore FAU-Y (7.4 × 7.4 × 7.4 $Å^3$) and LTL (7.5 × 2.1 × 2.1 $Å^3$) zeolites [42]. Conversely, strong homogeneous catalysts like sulfuric acid and hydrochloric acid experience full conversion of levulinic acid into propyl levulinate. Nevertheless, they are not reusable and the system has to undergo laborious neutralization, separation, and purification processes to isolate the reaction product [43]. For acetic acid, the conversion is the lowest (60.1%) due to its weak acidity.

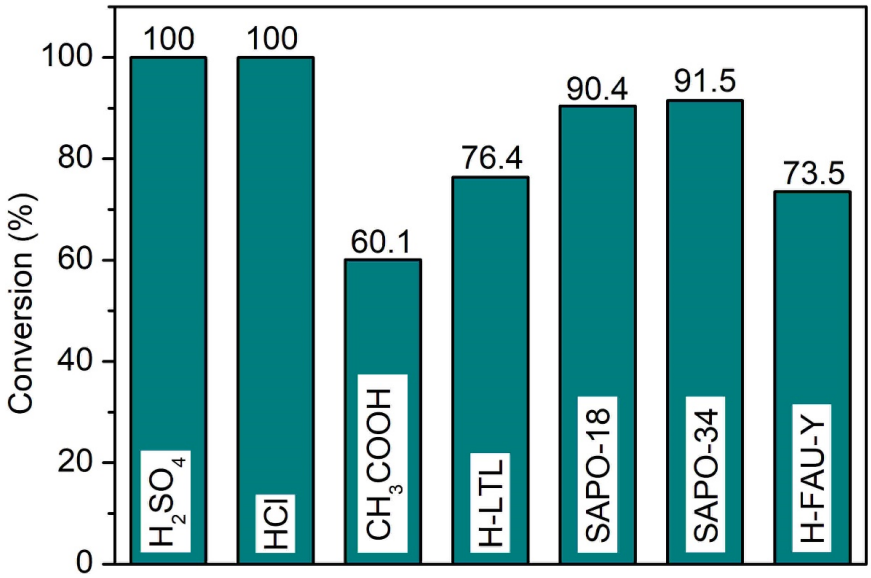

Figure 10. Catalytic performance of various homogeneous and heterogeneous acid catalysts in the esterification of levulinic acid with 1-propanol. Reaction conditions: Catalyst loading = 7.70 µmol equivalent to 0.100 g SAPO-34; 1-propanol:levulinic acid molar ratio = 11:1; reaction temperature = 190 °C; heating time = 20 min; microwave power = 800 W; solvent-free.

The major concern with heterogeneous catalysts is their stability and recyclability [44]. Hence, the catalyst recyclability of SAPO-34 was tested (Figure 11). The results reveal that the catalyst reactivity and stability are preserved even after five reaction cycles where an insignificant loss in conversion and selectivity are observed; a slight decrease in reaction conversion might be due to the physical loss of the catalyst during the recovery operation. Hence, SAPO-34 can be a promising eco-friendly and recyclable solid catalyst for the replacement of conventional homogeneous catalysts in biofuel synthesis in addition to being an efficient molecular sieve for gas separation.

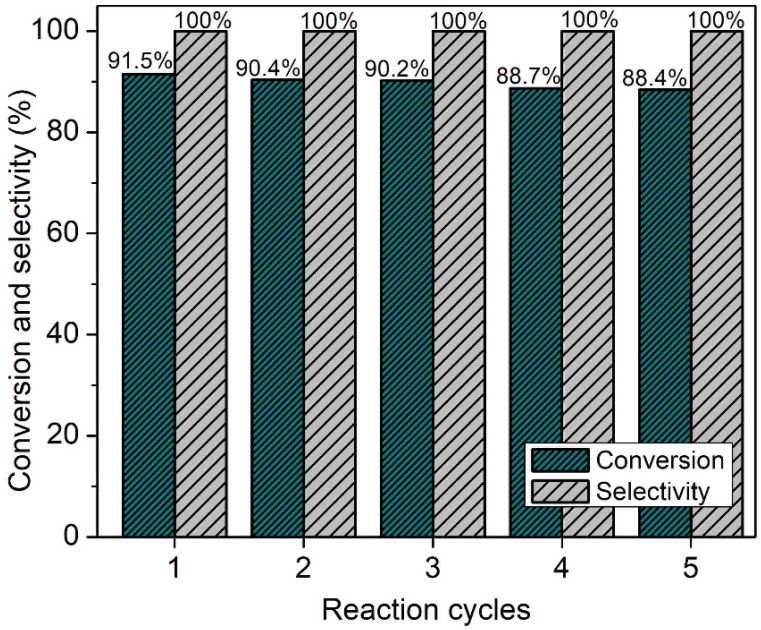

Figure 11. SAPO-34 catalyst reusability test after five reaction cycles.

3. Materials and Methods

3.1. Preparation of 1-Propylpyridinium Hydroxide, [PrPy]OH

Scheme 1 displays the synthesis procedure of the novel [PrPy]OH organic template. Typically, pyridine (82.20 g, 99%, Acros Organics, Geel, Belgium) and 1-bromopropane (191.71 g, 99%, Acros Organics, Geel, Belgium) were first mixed and heated under reflux for 18 h at 70 °C. The mixture was rotary evaporated under reduced pressure to remove excessive and unreacted 1-bromopropane, producing 1-propylpyridinium bromide ([PrPy]Br). The yellowish solid was soaked and purified with acetone (90 mL) several times prior to drying at 100 °C overnight to give an 87% yield of [PrPy]Br. The purity of [PrPy]Br was confirmed by ^{1}H and ^{13}C NMR, IR, and CHN analyses: ^{1}H NMR: δ (ppm) = 1.02 (triplet), 2.12 (multiplet), 4.70 (triplet), 8.18 (triplet), 8.65 (triplet), 8.97 (doublet). ^{13}C NMR: δ (ppm) = 10.25, 24.08, 63.73, 127.86, 144.02, 145.58. FTIR: ν (cm^{-1}) = 1169 (C–N), 1488 (C=N), 1503 & 1632 (C=C), 2878 ($C_{sp}{}^{3}$–H), 3054 ($C_{sp}{}^{2}$–H), 3405 (O–H). CHN analysis: $C_8H_{12}NBr$ theoretical = C, 47.54%; H, 5.95%; N, 6.92%; Experimental = C, 46.80%; H, 5.84%; N, 6.84%.

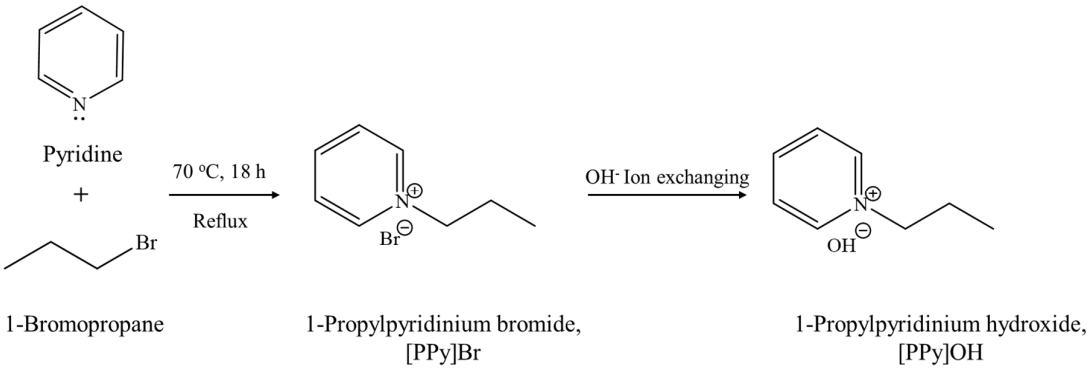

Scheme 1. The synthesis pathway of [PrPy]OH organic structural directing agent.

Subsequently, 50.00 g of both [PrPy]Br ionic liquid and Amberlite® IRN-78 OH^{-} resins (Acros Organics, Geel, Belgium) were mixed with 50.00 g of deionized water. The ion-exchange treatment was then performed at room temperature (17 h, 250 rpm). The template solution and the resins are isolated using vacuum filtration where the percentage

of OH^- ion exchange was confirmed by using 1.0 mL of the solution titrated with HCl (0.1 M). A similar ion-exchange procedure was performed until 87.0% OH^- exchange was achieved before allowing the sample to slowly concentrate to 32.8 wt.% in an electric oven (55 °C).

3.2. Single-Parameter Tuning Synthesis and Crystallization of SAPO-34 Microporous Solid

The synthesis of SAPO-34 microporous solid was conducted as follows: Aluminum triisopropoxide (0.6245 g, 98%, Sigma-Aldrich, Darmstadt, Germany) was first mixed with the [PrPy]OH template solution (4.5002 g) and stirred (600 rpm) for 30 min at room temperature. Afterward, deionized water (0.8350 g) was introduced. Then, orthophosphoric acid (0.8065 g, 85%, Acros Organics, Geel, Belgium) was slowly added whereby the entire addition process required 30 min. Lastly, tetraorthosilicate (0.2767 g, 98%. Sigma-Aldrich, Darmstadt, Germany) was introduced and stirred, forming a hydrogel mixture composed of 2.0 Al: 4.7 P: 6.7 [PrPy]OH: 0.9 Si: 148 H_2O molar composition. The mixture was loaded into an autoclave for crystallization at 200 °C for 19 h. The resulting solid product was washed with deionized water via centrifugation (9500 rpm, 8 min) until pH = 7 before being dried in an oven (70 °C, 16 h).

The effects of various parameters in the crystallization of SAPO-34 were also studied by varying one parameter of the synthesis conditions each time as summarized in Table 2 using similar preparation protocols. The samples were designated as S-*n* whereby *n* corresponded to the number of the sample.

Table 2. The hydrothermal crystallization conditions of SAPO-34 by varying the synthesis variables and the phase products obtained.

Entry	Variable Parameters	Hydrogel Composition in Molar Ratio					T (°C)	t (h)	pH before Synthesis	pH after Synthesis	Products *
		Al	P	Si	[PPy]	H_2O					
S-0	Crystallization time	2.0	4.7	0.9	6.7	148	200	6	6.68	6.75	No solid
S-1								12	6.72	6.80	Am
S-2								16	6.81	6.92	Am ≫ CHA
S-3								19	6.67	6.88	CHA
S-4								30	6.70	6.90	ATS ≫ CHA
S-5	P_2O_5	2.0	4.1	0.9	6.7	148	200	19	7.18	7.23	Am
S-3			4.7						6.67	6.88	CHA
S-6			5.3						6.18	6.77	CHA > AFI
S-7			5.9						5.61	6.34	AFI
S-8	SiO_2	2.0	4.7	0	6.7	148	200	19	6.76	7.00	Layered SAPO
S-9				0.5					7.06	7.15	ATS
S-3				0.9					6.67	6.88	CHA
S-10				1.4					6.86	7.00	LEV ≫ CHA
S-11	$[PPy]_2O$	2.0	4.7	0.9	5.3	148	200	19	5.76	6.79	AFI
S-12					6.0				6.31	6.64	AFI ≫ CHA
S-3					6.7				6.67	6.88	CHA
S-13					7.4				7.12	7.21	Am
S-14	H_2O	2.0	4.7	0.9	6.7	116	200	19	7.03	7.09	ATS ≫ CHA
S-3						148			6.67	6.88	CHA
S-15						180			6.55	6.86	ATS ≫ LEV > CHA
S-16						240			6.49	6.85	AFI ≫ ATS
S-17	Heating temperature	2.0	4.7	0.9	6.7	148	160	19	6.79	7.09	Am ≫ CHA
S-18							180		6.73	7.09	Am > CHA
S-3							200		6.67	6.88	CHA
S-19							220		6.80	6.44	ATS ≫ CHA

* Am = Amorphous, AFI = SAPO-5, ATS = SAPO-36, CHA = SAPO-34, LEV = SAPO-35.

3.3. Characterization

The elemental analysis of [PrPy]Br was performed using a Perkin Elmer 2400 Series II CHNS/O instrument (Waltham, MA, USA). The liquid ^{1}H and ^{13}C NMR spectra were acquired via a Bruker Advance 500 MHz spectrometer (Waltham, MA, USA) using a single pulse excitation with $\pi/2$ (3 μs) pulses, operating at 500 and 126 MHz, respectively. Deuterated oxide (D_2O) and tetramethylsilane (TMS) were used as the solvent and reference, respectively. The identity of the functional groups of [PrPy]Br was confirmed using a Perkin Elmer's System 2000 spectrometer (resolution 4 cm^{-1}, 50 scans, Waltham, MA, USA). The KBr pellet was prepared according to a KBr: sample weight ratio of 50:1. The crystallinity and zeolite phase composition were investigated using a Bruker D8 Advance diffractometer (Waltham, MA, USA) with copper Kα as the radiation source (λ = 0.154 nm at 40 kV and 10 mA, scanning rate 0.2° min^{-1}). The morphology and surface properties of solids were studied using a Hitachi Regulus 8220 FESEM microscope (Tokyo, Japan) at a voltage of 5 kV. The elemental composition of SAPO-34 (S-3 sample) was determined through a Phillips X'Unique XRF spectrometer (Cambridge, UK). The organic and inorganic moieties in the solid were studied using a Mettler TGA SDTA851 instrument (Columbus, OH, USA, heating rate of 20 °C min^{-1}) under a flow of air. The porous properties of SAPO-34 were investigated using a Micromeritics ASAP 2010 instrument (Norcross, GA, USA) at −196 °C. Before the analysis, ca. 0.080 g of calcined SAPO-34 powder was first degassed under vacuum at 250 °C for 6 h (to remove adsorbed impurities). The number and acid strength of synthesized SAPO-34 were investigated via BELCAT-B analyzer (York, PA, USA) using the NH_3-TPD technique. First, ca. 80 mg of calcined SAPO-34 sample was heated at 400 °C for 4 h under a helium flow of 30 cm^3 min^{-1}. Then, the solid was allowed to adsorb with NH_3. The excess NH_3 was removed by purging with helium for 20 min prior to initiating NH_3 desorption from 50 °C to 700 °C using a heating rate of 10 °C min^{-1}.

3.4. Catalytic Reaction Study

Esterification of levulinic acid and 1-propanol was used as a model reaction to study the catalytic performance of SAPO-34 (S-3 sample) under microwave heating (Monowave 200, Anton Paar, Graz, Austria). The resulting reaction product—propyl levulinate—is a very useful compound for biofuel applications [45]. First, the calcined SAPO-34 (0.100 g, 250 °C, 2 h) was mixed with levulinic acid (0.160 g, 1.34 mmol, 98%, Merck, Darmstadt, Germany) and 1-propanol (0.893 g, 14.7 mmol, 99%, Merck, Darmstadt, Germany) in a glass vessel. The resulting reaction mixture was stirred vigorously (500 rpm, 1 min) to ensure its homogeneity before heating to 160–190 °C for 0–60 min. The liquid product was separated using centrifugation (9000 rpm, 3 min) and subjected to qualitative and quantitative analyses using GC-MS (Agilent 7000 Series Triple Quad, Santa Clara, CA, USA) and GC-FID (Agilent's HP6890 GC, Santa Clara, CA, USA), respectively. For quantitative analysis, toluene was used as the internal standard. For the recyclability study, the spent catalyst after each cycle was soaked and washed with diethyl ether five times (10 mL) before re-activation. A similar catalytic reaction procedure was repeated for the next four cycles.

4. Conclusions

In conclusion, the effects of synthesis variables on the crystallization of SAPO-34 in the presence of a 1-propylpyridinium hydroxide ([PrPy]OH) template have been systematically investigated. The findings show that the nucleation, crystallization, structural purity and metastability, crystallite size, and morphology are strongly affected by the synthesis conditions of SAPO-34, namely, the chemical composition of the initial precursor gel, heating temperature, and heating duration. During the course of the slight altering of the synthesis parameters, SAPO-5 (AFI), SAPO-35 (LEV), and SAPO-36 (ATS) as the common competing phases are observed. More specifically, the pH of the precursor gel influences the final zeolite phase where SAPO-34 favors a nearly neutral precursor gel (pH = 6.6–6.8) while SAPO-5 tends to predominate at lower pH values (pH = 5.6–5.8). Meanwhile, SAPO-36 forms at lower

silicon content, higher crystallization temperatures, and longer heating times due to its higher metastability and denser framework nature whereas SAPO-35 can only form at high silicon content as revealed in the parameter effects study. In addition, the [PrPy]OH SDA not only helps in forming a highly crystalline SAPO-34 zeolite structure but is also an SDA for SAPO-5 in a weakly acidic environment. Nevertheless, a precise water content (H_2O/Al = 74) is very important to ensure the crystallization of pure SAPO-34. Lastly, the SAPO-34 zeolite synthesized using [PrPy]OH is also catalytically active in the synthesis of propyl levulinate via esterification reaction where it shows 91.5% of conversion in only 20 min when heated at 190 °C under microwave heating conditions. Hence, this study provides insights into the structural-directing ability and selectivity of the novel [PrPy]OH organic template under various synthesis parameters. In addition to being reusable, the prepared SAPO-34 hence provides a promising green alternative for the economical and sustainable production of renewable fuel blending levulinate compound.

Supplementary Materials: The following supporting information can be downloaded at: https://www.mdpi.com/article/10.3390/catal13040680/s1, Table S1: Physicochemical properties of various zeolites.

Author Contributions: Conceptualization, T.S.A., N.A. and E.-P.N.; methodology, Y.-K.M.; software, T.S.A. and N.A.; formal analysis, Y.-K.M., T.J.D. and E.-P.N.; investigation, Y.-K.M., T.J.D. and F.K.; resources, S.C.; data curation, T.J.D.; writing—original draft preparation, Y.-K.M.; writing—review and editing, Z.M.E.-B. and E.-P.N.; supervision, T.C.L. and E.-P.N.; project administration, T.S.A., N.A. and E.-P.N.; funding acquisition, T.S.A., N.A. and E.-P.N. All authors have read and agreed to the published version of the manuscript.

Funding: Fundamental Research Grant Scheme (FRGS/1/2022/STG05/USM/02/12, Ministry of Higher Education of Malaysia), and Princess Nourah bint Abdularahman University Researchers Supporting Project number (PNURSP2023R47), Princess Nourah bint Abdularahman University, Riyadh, Saudi Arabia.

Acknowledgments: The authors would like to acknowledge the Fundamental Research Grant Scheme (FRGS/1/2022/STG05/USM/02/12, Ministry of Higher Education of Malaysia) for financial support. The authors also acknowledge the financial support from Princess Nourah bint Abdularahman University Researchers Supporting Project number (PNURSP2023R47), Princess Nourah bint Abdularahman University, Riyadh, Saudi Arabia.

Conflicts of Interest: The authors declare no conflict of interest.

References

1. Ng, E.-P.; Awala, H.; Komaty, S.; Mintova, S. Microwave-green synthesis of AlPO-n and SAPO-n (n = 5 and 18) nanosized crystals and their assembly in layers. *Microporous Mesoporous Mater.* **2019**, *280*, 256–263. [CrossRef]
2. Tosheva, L.; Ng, E.-P.; Mintova, S.; Hölzl, M.; Metzger, T.H.; Doyle, A.M. $AlPO_4$-18 Seed Layers and Films by Secondary Growth. *Chem. Mater.* **2008**, *20*, 5721–5726. [CrossRef]
3. Ng, E.-P.; Delmotte, L.; Mintova, S. Selective capture of water using microporous adsorbents to increase the lifetime of lubricants. *ChemSusChem* **2009**, *2*, 255–260. [CrossRef] [PubMed]
4. Usman, M. Recent Progress of SAPO-34 Zeolite Membranes for CO_2 Separation: A Review. *Membranes* **2022**, *12*, 507. [CrossRef]
5. Park, J.W.; Lee, J.Y.; Kim, K.S.; Hong, S.B.; Seo, G. Effects of cage shape and size of 8-membered ring molecular sieves on their deactivation in methanol-to-olefin (MTO) reactions. *Appl. Catal. A Gen.* **2008**, *339*, 36–44. [CrossRef]
6. Zhao, L.; Yang, G.; Hu, H.; Sun, Y.; Ma, Z.; Peng, P.; Ng, E.-P.; Tian, P.; Guo, H.; Mintova, S. SAPO-34 crystals with nanosheet morphology synthesized by pyrophosphoric acid as new phosphorus source. *Microporous Mesoporous Mater.* **2022**, *333*, 111753. [CrossRef]
7. Nishitoba, T.; Nozaki, T.; Park, S.; Wang, Y.; Kondo, J.N.; Gies, H.; Yokoi, T. CHA-type zeolite prepared by interzeolite conversion method using FAU and LTL-type zeolite: Effect of the raw materials on the crystallization mechanism, and physico-chemical and catalytic properties. *Catalysts* **2020**, *10*, 1204. [CrossRef]
8. Li, J.; Li, Z.; Han, D.; Wu, J. Facile synthesis of SAPO-34 with small crystal size for conversion of methanol to olefins. *Powder Technol.* **2014**, *262*, 177–182. [CrossRef]
9. Liu, G.; Tian, P.; Liu, Z. Chin. Synthesis of SAPO-34 molecular sieves templated with diethylamine and their properties compared with other templates. *J. Catal.* **2012**, *33*, 174–182.

10. Zhou, H.; Wang, Y.; Wei, F.; Wang, D.; Wang, Z. Kinetics of the reactions of the light alkenes over SAPO-34. *Appl. Catal. A Gen.* **2008**, *348*, 135–141. [CrossRef]
11. Askari, S.; Halladj, R.; Sohrabi, M. Methanol conversion to light olefins over sonochemically prepared SAPO-34 nanocatalyst. *Microporous Mesoporous Mater.* **2012**, *163*, 334–342. [CrossRef]
12. Dumitriu, E.; Azzouz, A.; Hulea, V.; Lutic, D.; Kessler, H. Synthesis, characterization and catalytic activity of SAPO-34 obtained with piperidine as templating agent. *Microporous Mesoporous Mater.* **1997**, *10*, 1–12. [CrossRef]
13. Prakash, A.M.; Unnikrishnan, S. Synthesis of SAPO-34: High silicon incorporation in the presence of morpholine as template. *J. Chem. Soc. Faraday Trans.* **1994**, *90*, 2291–2296. [CrossRef]
14. Ng, E.-P.; Itani, L.; Sekhon, S.S.; Mintova, S. Micro- to macroscopic observations of MnAlPO-5 nanocrystal growth in ionic-liquid media. *Chem. Eur. J.* **2010**, *16*, 12890–12897. [CrossRef]
15. Khoo, D.Y.; Kok, W.-M.; Mukti, R.R.; Mintova, S.; Ng, E.-P. Ionothermal approach for synthesizing AlPO-5 with hexagonal thin-plate morphology influenced by various parameters at ambient pressure. *Solid State Sci.* **2013**, *25*, 63–69. [CrossRef]
16. Smith, J.G. *Organic Chemistry*, 6th ed.; McGraw-Hill Education: New York, NY, USA, 2017.
17. Majano, G.; Ng, E.-P.; Lakiss, L.; Mintova, S. Nanosized molecular sieves utilized as an environmentally friendly alternative to antioxidants for lubricant oils. *Green Chem.* **2011**, *13*, 2435–2440. [CrossRef]
18. Wong, J.-T.; Ng, E.-P.; Adam, F. Microscopic Investigation of Nanocrystalline Zeolite L Synthesized from Rice Husk Ash. *J. Am. Ceram. Soc.* **2011**, *95*, 805–808. [CrossRef]
19. Cundy, C.S.; Cox, P.A. The hydrothermal synthesis of zeolites: Precursors, intermediates and reaction mechanism. *Microporous Mesoporous Mater.* **2005**, *82*, 1–78. [CrossRef]
20. Auwal, I.; Khoerunnisa, F.; Dubray, F.; Mintova, S.; Ling, T.; Wong, K.-L.; Ng, E.-P. Effects of Synthesis Parameters on the Crystallization Profile and Morphological Properties of SAPO-5 Templated by 1-Benzyl-2,3-Dimethylimidazolium Hydroxide. *Crystals* **2021**, *11*, 279. [CrossRef]
21. Van Heyden, H.; Mintova, S.; Bein, T. Nanosized SAPO-34 Synthesized from Colloidal Solutions. *Chem. Mater.* **2008**, *20*, 2956–2963. [CrossRef]
22. Zhao, C.; Yang, Y.; Chen, W.; Wang, H.; Zhao, D.; Webley, P.A. Hydrothermal synthesis of novel AlPO4-5 brooms and nano-fibers and their templated carbon structures. *CrystEngComm* **2009**, *11*, 739–742. [CrossRef]
23. IZA-SC Database of Zeolite Structures. Available online: https://www.izastructure.org/databases/ (accessed on 5 July 2022).
24. Barthomeuf, D. Topological model for the compared acidity of SAPOs and SiAl zeolites. *Zeolites* **1994**, *14*, 394–401. [CrossRef]
25. Salmasi, M.; Fatemi, S.; Hashemi, S. MTO reaction over SAPO-34 catalysts synthesized by combination of TEAOH and morpholine templates and different silica sources. *Sci. Iran.* **2012**, *19*, 1632–1637. [CrossRef]
26. Baerlocher, C.; Meier, W.M.; Olson, D.H. *Atlas of Zeolite Structure Types*, 5th ed.; Elsevier: Amsterdam, The Netherlands, 1996.
27. Concepción, P.; Nieto, J.M.L.; Mifsud, A.; Perez-Pariente, J. Preparation and characterization of Mg-containing AFI and chabazite-type materials. *Zeolites* **1996**, *16*, 56–64. [CrossRef]
28. *The Molecular Dimension of 1-Propylpyridinium Cation Was Estimated Using Hyperchem™-Release 7.03 for Windows Molecular Modeling System*; Hypercube, Inc.: Lancaster, TX, USA, 2002.
29. Newalkar, B.L.; Kamath, B.V.; Jasra, R.V.; Bhat, S.G.T. The effect of gel pH on the crystallization of aluminophosphate molecular sieve AlPO4-5. *Zeolites* **1997**, *18*, 286–290. [CrossRef]
30. Ghrear, T.M.A.; Rigolet, S.; Daou, T.J.; Mintova, S.; Ling, T.C.; Tan, S.H.; Ng, E.-P. Synthesis of Cs-ABW nanozeolite in organotemplate-free system. *Microporous Mesoporous Mater.* **2019**, *277*, 78–83. [CrossRef]
31. Cheong, Y.-W.; Rigolet, S.; Daou, T.J.; Wong, K.-L.; Ling, T.C.; Ng, E.-P. Crystal growth study of nanosized K-MER zeolite from bamboo leaves ash and its catalytic behaviour in Knoevenagel condensation of benzaldehyde with ethyl cyanoacetate. *Mater. Chem. Phys.* **2020**, *251*, 123100. [CrossRef]
32. Jhung, S.H.; Chang, J.-S.; Hwang, J.S.; Park, S.-E. Selective formation of SAPO-5 and SAPO-34 molecular sieves with micro-wave irradiation and hydrothermal heating. *Microporous Mesoporous Mater.* **2003**, *64*, 33–39. [CrossRef]
33. Newsam, J.M. The Zeolite Cage Structure. *Science* **1986**, *231*, 1093–1099. [CrossRef]
34. Cundy, C.S.; Cox, P.A. The Hydrothermal Synthesis of Zeolites: History and Development from the Earliest Days to the Present Time. *Chem. Rev.* **2003**, *103*, 663–702. [CrossRef]
35. Francis, R.J.; O'Hare, D. The kinetics and mechanisms of the crystallisation of microporous materials. *J. Chem. Soc. Dalton Trans.* **1998**, 3133–3148. [CrossRef]
36. Wong, S.-F.; Deekomwong, K.; Wittayakun, J.; Ling, T.C.; Muraza, O.; Adam, F.; Ng, E.-P. Crystal growth study of K-F nanozeolite and its catalytic behavior in Aldol condensation of benzaldehyde and heptanal enhanced by microwave heating. *Mater. Chem. Phys.* **2017**, *196*, 295–301. [CrossRef]
37. Askari, S.; Halladj, R.; Sohrabi, M. An overview of the effects of crystallization time, template and silicon sources on hydro-thermal synthesis of sapo-34 molecular sieve with small crystals. *Rev. Adv. Mater. Sci.* **2012**, *32*, 83–93.
38. Kruk, M.; Jaroniec, M.; Sayari, A. Adsorption Study of Surface and Structural Properties of MCM-41 Materials of Different Pore Sizes. *J. Phys. Chem. B* **1997**, *101*, 583–589. [CrossRef]
39. Derewinski, M.; Briend, M.; Peltre, M.J.; Main, P.P.; Barthomeuf, D. Changes in the environment of si and ai in SAPO-37 zeolite during acidity measurements. *J. Phys. Chem.* **1993**, *97*, 13730–13735. [CrossRef]

40. Silbey, R.J.; Alberty, R.A.; Papadantonakis, G.A.; Bawendi, M.G. *Physical Chemistry*, 5th ed.; John, Wiley & Sons, Inc.: Hoboken, NJ, USA, 2022.
41. Beh, J.J.; Lim, J.K.; Ng, E.P.; Ooi, B.S. Synthesis and size control of zeolitic imidazolate framework-8 (ZIF-8): From the perspective of reaction kinetics and thermodynamics of nucleation. *Mater. Chem. Phys.* **2018**, *216*, 393–401. [CrossRef]
42. Li, T.; Chung, S.-H.; Nastase, S.; Galilea, A.; Wang, Y.; Mukhambetov, I.; Zaarour, M.; de Miguel, J.C.N.; Cazemier, J.; Dokania, A.; et al. Influence of active-site proximity in zeolites on Brønsted acid-catalyzed reactions at the microscopic and mesoscopic levels. *J. Chem. Catal.* **2023**, *3*, 100540. [CrossRef]
43. Mandari, V.; Devarai, S.K. Biodiesel production using homogeneous, heterogeneous, and enzyme catalysts via transesterification and esterification reactions: A critical review. *BioEnergy Res.* **2022**, *15*, 935–961. [CrossRef]
44. Shokouhimehr, M. Magnetically separable and sustainable nanostructured catalysts for heterogeneous reduction of nitroaromatics. *Catalysts* **2015**, *5*, 534–560. [CrossRef]
45. Appaturi, J.N.; Andas, J.; Ma, Y.-K.; Phoon, B.L.; Batagarawa, S.M.; Khoerunnisa, F.; Hussin, M.H.; Ng, E.-P. Recent advances in heterogeneous catalysts for the synthesis of alkyl levulinate biofuel additives from renewable levulinic acid: A comprehensive review. *Fuel* **2022**, *323*, 124362. [CrossRef]